Power Analysis in an SMC-Based Aerospace Transverse Flux Generator for Different Load and Speed Conditions

Víctor Ballestín-Bernad, Mehmet C. Kulan, Nick J. Baker, *Member, IEEE*, José Antonio Domínguez-Navarro, *Senior Member, IEEE*

***Abstract*—Transverse flux machines (TFMs) with independent phases are suitable for aerospace applications, where fault-tolerance is required. Their complex 3D flux path can be accommodated by using soft magnetic composites (SMC). However, core loss evaluation of SMC-based electrical machines is limited by the accuracy of calculation models, most of which have been applied under no-load conditions. Therefore, the aim of this paper is to compare experimental power and losses in an SMC-based TFM with results given by the equivalent circuit and the finite element method, thus providing a better insight of loss mechanisms. At 5000 r/min results show a good agreement, however, at 400 r/min experimental power on the load is lower than expected for high power values. Further measurements and analysis indicate that great iron losses are affecting power production at low speeds. Therefore, choosing a high-resistivity SMC material for the stator cores, with a good performance regarding high-speed losses, may entail some uncertainties for low-speed operation due to the magnetic behavior of SMC under load conditions.**

***Index Terms*—transverse flux machines, soft magnetic composites, aerospace generator, permanent magnet machines, finite element method**

I. Introduction

Transverse flux machines (TFMs) are a well-known solution for those applications in which high torque density is desired, such as electric vehicles, wind turbines and fault-tolerant aircraft generators [1], [2]. TFMs are mostly based on single-phase structures that are stacked in the axial direction, thus leading to multi-phase arrangements. Some advantages of the modular construction include enhanced manufacturability and simplified repairing [3]. Each single-phase stack is formed by a hoop-shaped coil, surrounded by a number of ferromagnetic cores that guide the magnetic flux through the stator and the rotor. This feature makes TFMs unique, as the hoop-shaped coil encompasses the flux linkage of all the pole pairs, leading to high torque and back electromotive force (back-EMF) ratings [4], [5]. Besides, in most TFM topologies the rotor has permanent magnets (PMs), therefore these machines operate commonly as permanent magnet synchronous machines. Moreover, TFMs exhibit good fault-tolerance capabilities via two mechanisms: the physical separation between segmented phases and the high inductance that limits short-circuit current [6], [7].

Additive manufacturing (AM) has been recently introduced in the field of electrical machines in order to overcome the limitations of traditional manufacturing techniques and their effects on electric drives design and performance. AM offers a broad range of benefits over conventional manufacturing techniques, such as optimal material utilization, improved thermal and mechanical performance, complex shape realizations, size and weight reduction and control over physical properties of the materials [8]. In terms of the level of technology maturity, AM of active components is still behind structural and thermal management implementations [9]. Soft magnetic composites (SMC), made from pressed iron particles that are magnetically insulated from each other, are known as the most appropriate active material for realization of innovative core structures, due to their unique properties, such as magnetic and thermal isotropy, low eddy current losses at high frequencies, and the prospect of low-cost mass production [10]. Nevertheless, they suffer from higher hysteresis losses and lower magnetic permeability than conventional ferromagnetic materials [11].

As TFMs usually have a complex structure, with a large number of ferromagnetic pieces, AM opens up new possibilities for magnetic core designs based on SMC [12]–[16], as well as structural improvements given by flexibility of 3D printing [17]–[20]. Regarding the magnetic core design, some authors indicate that SMC-based electrical machines exhibit higher experimental losses than those computed by the finite element method (FEM) [21]–[24], therefore loss characterization is a major concern in order to improve accuracy when designing electrical machines with SMC.

The literature presents different methods to calculate iron losses in electrical machines [25], [26]. In case of SMC materials, the inclusion of rotational losses in loss equations is of great importance, as specific rotational losses can be higher than their alternating counterpart [27]. Authors in [28] propose an iron loss model based on a three-term equation that includes the effects of rotational components of the magnetic field, as well as higher-order harmonics. The model has been applied to loss computations of a claw-pole machine [21]–[23] and a transverse flux machine [29], [30].

Manuscript created June, 2024.
This work was partially done during a research stay at Newcastle University, supported in part by the Spanish Ministry of Universities under grant FPU20/03436. The authors gratefully acknowledge UK government funding to carry out this research, under Innovate Grant 76019, part of the Driving Electric Revolution (DER) initiative.
Víctor Ballestín-Bernad and José Antonio Domínguez-Navarro are with the Department of Electrical Engineering, University of Zaragoza, 50018 Zaragoza, Spain (email: ballestin@unizar.es, jadona@unizar.es).
Mehmet C. Kulan and Nick J. Baker are with the School of Engineering, Newcastle University, Newcastle Upon Tyne, United Kingdom (email: Mehmet.Kulan@newcastle.ac.uk, nick.baker@newcastle.ac.uk).

Although it is well-known that the armature reaction significantly affects the magnetic field, and therefore iron losses, among previous references only [30] includes core loss results under full-load conditions, whereas [21]–[23], [29] present no-load core losses exclusively. Thereby, the effects of partial loads at different speeds in electrical machines with SMC materials are still unknown. This paper provides a better insight of loss mechanisms in an SMC-based TFM, comparing experimental results with those given by FEM and the equivalent circuit (EC). Furthermore, the innovative structure of the TFM, with four independent phases formed by C-shaped cores and flux-concentrating magnets, makes the assembly and modeling being unique, as discussed in [15], [16].

This paper is structured as follows. In Section II the main characteristics of the proposed transverse flux generator for aerospace applications are presented, as well as the experimental determination of the equivalent circuit. In Section III power computations and tests at low and medium speeds for different loads are described, comparing results given by the equivalent circuit, the finite element method and experiments. Section IV presents a deeper analysis of low-speed losses on the TFM. Finally, Section V concludes the paper.

II. SMC Transverse Flux Generator for Aerospace Applications

A. Design and Prototyping

The TFM that is analyzed and tested in this work is intended to work in civil aviation as a fault-tolerant generator within the auxiliary power unit, i.e. a small jet engine that provides electric and pneumatic power when the main engines are not running. The electric generator provides a redundant power supply to the Full Authority Digital Engine Control (FADEC) electronics and actuators, being direct-driven from the engine gearbox via a dedicated low speed output and delivering constant power across a wide engine speed range [31].

Fig. 1 shows a single-phase overview of the proposed TFM [15], [16]. The stator and the rotor are formed by soft magnetic composite (SMC) cores that embrace each single-phase hoop-shaped coil of the stator, thus guiding the magnetic field. This stator core is known as a C-shaped core, according to the classification proposed in [1]. The rotor is formed by flux-concentrating SmCo magnets that are retained by a carbon fiber sleeve against centrifugal forces. SmCo magnets operate better than NdFeB magnets at higher temperatures and in more corrosive environments [32], this being a critical attribute for maintaining functionality in the demanding environmental conditions of aerospace operations. The rotor hub and the rotor shaft, made of a Titanium alloy and steel respectively, are for mechanical support and are not part of the magnetic circuit. The utilization of innovative segmented stator technology with SMC components makes the prototype of this aerospace alternator expensive, however, mass manufacturing of the proposed alternator will substantially save costs, as it eliminates leftover components often seen in electrical machines with laminated steels, and the proposed machine's windings consist of simple hoop coils rather than single tooth windings.

The main design specifications and target values of the TFM are shown in Table I [15]. The machine is formed by four independent phases that are shifted 90 electrical degrees. Besides, the TFM has two rated speeds, 400 r/min and 15000 r/min, and 12 pole pairs, thus leading to 80 Hz and 3 kHz rated frequencies. Furthermore, the number of turns is different in each single-phase stack ($N_1 = 26$ turns in phases 1 and 4, and $N_2 = 20$ turns in phases 2 and 3) in order to balance short-circuit currents as the central phases (Phase-2 and Phase-3) utilize higher mutual flux linkage in comparison to end phases (Phase-1 and Phase-4).

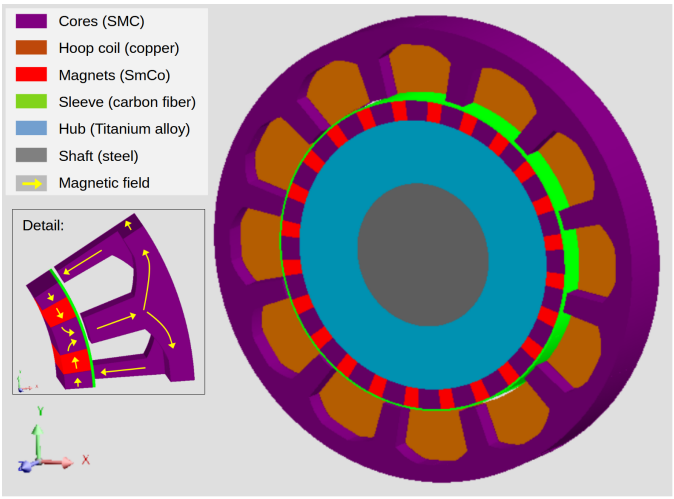

Figure 1: Single-phase overview of the proposed TFM and detail of the magnetic field path

Table I: Design specifications and target values of the transverse flux generator

Number of phases, m	4
Number of pole pairs, p	12
Rated, low speed	400 r/min
Rated, high speed	15000 r/min
Stator outer diameter	$\leq$ 160 mm
Active stack length	$\leq$ 100 mm
RMS Back-EMF at 15000 r/min	$\leq$ 265 V
RMS short circuit current at 15000 r/min	$\leq$ 25 A
Power per phase at 400 r/min	$\geq$ 40 W
Power per phase at 15000 r/min after a passive rectifier	$\geq$ 1200 W

The prototype is shown in Fig. 2. The rotor outer diameter is 110 mm and the air gap length is 0.8 mm. In previous work the topology was optimized for maximum power output using the response surface method [15], and then the effect of combining the four phases in a single stack was investigated [16]. Moreover, in [24] a preliminary insight into power calculation was presented, but computational results did not show a good accuracy when compared with experimental tests.

B. Equivalent Circuit

Fig. 3 illustrates the equivalent circuit of a permanent magnet synchronous machine (PMSM). Initialy, no iron losses will be considered, as commonly done, so the core loss resistor R_{Fe} fulfills $R_{Fe} \to \infty$. Therefore, the main parameters to be determined in order to characterize the generator performance are: the back-EMF E_0, i.e. the induced voltage with no load, the synchronous reactance X_s and the stator resistance R_s.

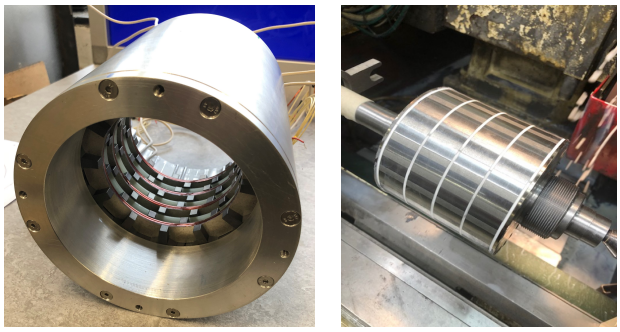

(a) (b)

Figure 2: TFM prototype: (a) stator, (b) rotor view without the carbon fiber sleeve

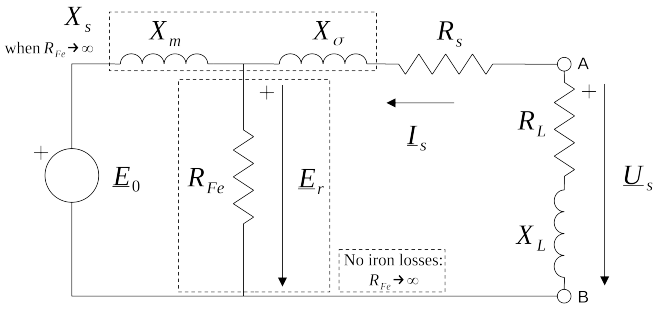

Figure 3: Equivalent circuit of a PMSM

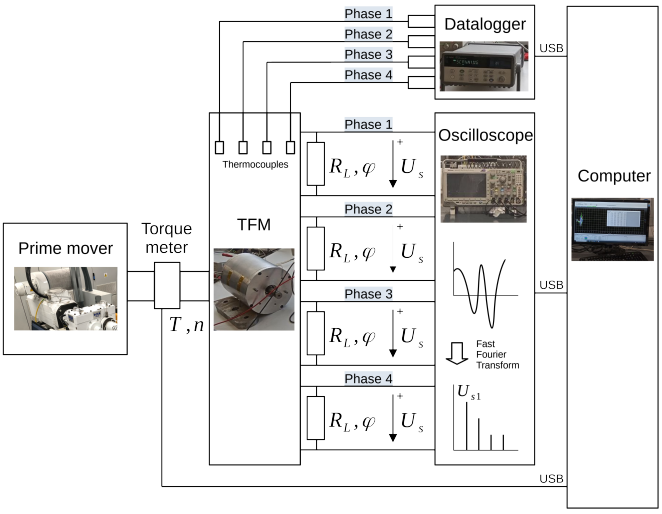

(a)

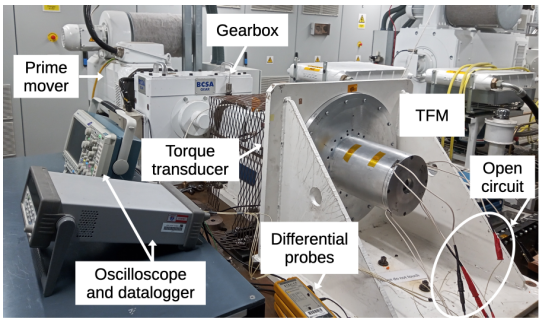

(b)

Figure 4: Experimental setup: (a) General scheme, (b) Instruments for open-circuit tests

The synchronous reactance is defined as the sum of the magnetizing reactance X_m and the leakage reactance X_σ. In case of under-load operation, the resistive and inductive components of the load, R_L and X_L, have also to be determined.

1) DC Current Tests, Stator Resistance: The stator resistance has been determined experimentally. Current-controlled sources introduce DC currents I_{DC} in the TFM and then the terminal voltage of the source U_{DC} is recorded with an Agilent 34972a data logger, so the stator resistance R_s is given by Ohm's law (1). Correlating resistance values with the temperature rise, that is measured using K-type thermocouples embedded in the stator slots, the rated resistance values at 20 °C can be obtained. More details about the experimental procedure and results can be found in [24].

$$R_s = \frac{U_{DC}}{I_{DC}} \tag{1}$$

2) Open-Circuit and Short-Circuit Tests, Synchronous Impedance: Open-circuit and short-circuit tests have been conducted on the proposed TFM, using the test rig illustrated in Fig. 4. This is a 100 kW test rig rated up to 30000 r/min. When the prime mover drives the TFM at a given speed, mechanical torque T and speed n are recorded through the torque transducer, and electrical magnitudes such as voltage and current are registered by the digital oscilloscope. More precisely, open circuit tests give the total no-load losses and the back-EMF, and short circuit tests give the short-circuit current (SCC). Furthermore, temperature measurements from the thermocouples can be recorded over time using a datalogger.

According to the IEC Standards for synchronous machines characterization [33], the synchronous reactance X_s is determined as the quotient between the back-EMF and the SCC at rated speed, provided that the armature resistance is lower than 0.2 of the synchronous reactance. As this condition is not fulfilled in the proposed TFM at rated low-speed (400 r/min), a different procedure will be used. Moreover, first-order harmonics shall be considered, say E_{01} for the back-EMF and I_{SC1} for the SCC. The RMS back-EMF first harmonic has been found to be linear with speed in the TFM throughout the whole speed range, up to 15000 r/min.

Fig. 5 illustrates the back-EMF waveforms of the four phases at 400 r/min and their first harmonics, it is shown that the first harmonic amplitudes are close but not equal to the peak values. Moreover, the back-EMFs of phases 1 and 4 differ from phases 2 and 3 because the number of turns is not the same, as stated in Section II-A.

In order to determine the synchronous reactance in the most general case, when the stator resistance cannot be neglected, a curve-fitting approach has been used. Firstly, open-circuit and short-circuit tests at different speeds give the synchronous impedance Z_s (2). As the stator resistance R_s has been measured and the synchrouous reactance X_s is a function

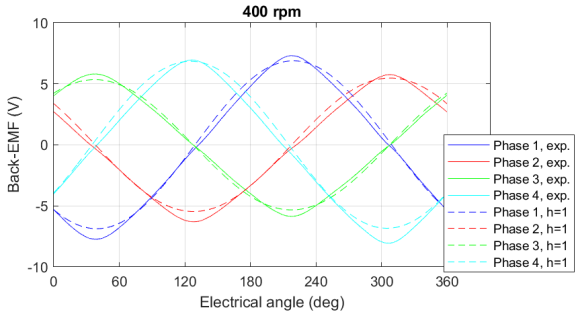

Figure 5: Back-EMF at 400 r/min: experimental waveforms (solid lines) and first-harmonics (dashed lines)

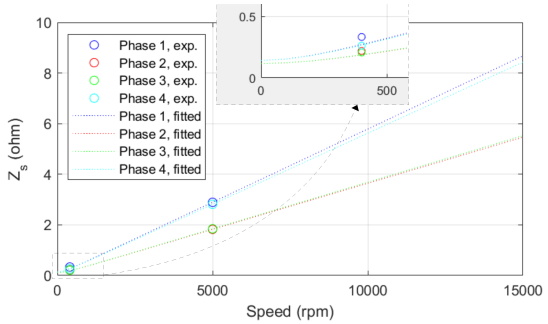

Figure 6: Curve-fitting of the synchronous impedance versus speed

of speed n in r/min and synchronous inductance L_s (3), the synchronous inductance can be determined as an independent parameter of speed from Z_s via curve-fitting (4).

$$Z_s(n) = \frac{E_{01}(n)}{I_{SC1}(n)} \tag{2}$$

$$X_s(n) = L_s\omega = \frac{2\pi p}{60} L_s n \tag{3}$$

$$Z_s(n) = \sqrt{R_s^2 + X_s^2(n)} \tag{4}$$

Fig. 6 shows the results from experimental tests at 400 r/min and 5000 r/min: at medium and high speeds the inductive reactance is the main component of impedance so Z_s is linear with speed, however, at low speeds near 400 r/min there is a significant effect of the stator resistance and impedance becomes nonlinear with speed. Table II shows more details about the parameters of the equivalent circuit from open-circuit and short-circuit tests, where it is clearly shown that the stator resistance cannot be neglected at lower speeds as it is the main contribution to synchronous impedance.

C. Finite Element Model

3D FEM simulations have been computed using Altair Flux. A single pole pair of a single phase has been modeled, using tetrahedral, second-order elements. Boundary conditions are: periodicity along pole pairs in the circumferential direction and zero magnetic field in infinity by use of an infinite box technique. Regarding the materials properties, nonlinear B-H curves of SMC materials have been introduced, furthermore,

Table II: Parameters of the equivalent circuit

Parameter	Phase 1	Phase 2	Phase 3	Phase 4
$E_{01(EC)}$ (V) at 400 r/min	4.8	3.8	3.8	4.9
$E_{01(EC)}$ (V) at 5000 r/min	59.4	47.7	47.1	60.7
R_s (ohm) at 20 °C	0.1420	0.1170	0.1170	0.1420
L_s (uH)	460	290	293	447
X_s (ohm) at 400 r/min	0.2314	0.1457	0.1473	0.2248
X_s (ohm) at 5000 r/min	2.8927	1.8214	1.8419	2.8103
R_s/X_s at 400 r/min	0.61	0.80	0.79	0.63
R_s/X_s at 5000 r/min	0.05	0.06	0.06	0.05

the rotor hub and PMs are modeled as solid conducting regions in order to compute Joule losses, and in case of Joule losses in the winding the experimental value of the resistance has been introduced instead. Then iron losses calculation has been conducted in postprocessing using a dedicated script. This script implements an empirical three-term model, based on [28], that aggregates alternating and rotational losses given by the harmonic decomposition of the flux density. Simulations have been conducted over several electric periods for different loads and speeds, coupling FEM model and the circuit model of the load. The measured loads obtained using a static motor analyzer (Baker Instrument by SKF) have been utilised. FEM software calculates the field distribution and then Joule losses in conducting regions, as well as active power on the load.

III. Power Computations in a Transverse Flux Generator for Different Loads and Speeds

A. Selection of the Loads and Experimental Tests

The TFM has been tested for different loads at 400 r/min and 5000 r/min, i.e. for low and medium speeds. The experimental setups are based on adjustable resistive loads R_L, as shown in Fig. 7. For low-speed tests, a collection of resistors has been selected, changing the connections from series to parallel in each case. On the other hand, for medium-speed tests four variable resistors are utilized instead. The generator is operating alone, so the power factor is imposed by the load. Resistors of low-speed tests have a unity power factor, however, it has been checked experimentally using a static analyzer that the rheostats utilized in medium-speed tests have a parasitic inductance, their power factor being near 0.9.

According to the equivalent circuit of a synchronous machine, that neglects iron losses, maximum power transfer from the generator to the load gives (5). If the inductive component of the load impedance is assumed to be null, $X_L \approxeq 0$, the condition for maximum power transfer is then reduced to (6) at each particular speed.

$$\frac{\partial P_L}{\partial R_L} = 0 \Rightarrow R_L^2 = R_s^2 + (X_s + X_L)^2 \tag{5}$$

$$R_L = Z_s \tag{6}$$

Besides, the torquemeter records the torque T applied to the generator shaft, therefore experimental input power P_{in} follows (7).

$$P_{in} = \frac{2\pi}{60} T n \tag{7}$$

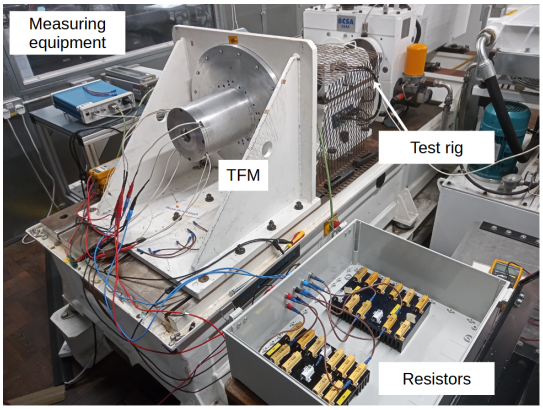

(a)

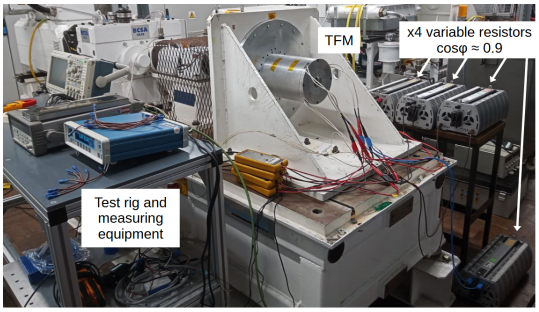

(b)

Figure 7: Experimental setup for load tests: (a) 400 r/min, (b) 5000 r/min

Furthermore, four-phase experimental power on the load P_{L4} is given by the stator voltage and the load parameters at each phase, then adding up the contribution of all phases (8). The stator voltage of each phase is recorded by the digital oscilloscope, so the RMS value of its first harmonic U_{s1} can be determined using Fourier series. Besides, the load is characterized at each phase with a static analyzer, being R_L its resistive component and $\cos\varphi$ its power factor.

$$P_{L4} = \sum_{m=1}^{4} \frac{U_{s1}^2 \left(\cos\varphi\right)^2}{R_L} \tag{8}$$

Joule losses in the stator resistance P_{s4} are given by (9), and power balance follows (10), where P_σ denotes other loss components, such as Joule losses on PMs and the rotor hub region, as well as iron loses in SMC materials and mechanical losses.

$$P_{s4} = \sum_{m=1}^{4} \frac{U_{s1}^2 R_s}{R_L^2 + X_L^2} \tag{9}$$

$$P_{in} = P_{L4} + P_{s4} + P_\sigma \tag{10}$$

B. Power Computations Using the Equivalent Circuit With No Iron Losses

According to the single-phase circuit of the synchronous machine (Fig. 3), when iron losses are neglected as in conventional analytical approaches, active power on the load $P_{L4(EC)}$ is given by (11), where the contribution of all the phases has been added up. The RMS back-EMF, first harmonic $E_{01(EC)}$ is generally assumed to be linear with speed (12). Besides, the resistive load has been selected to match the synchronous impedance for different R_L/Z_s values each speed. In case of medium-speed tests, a load power factor of 0.9 has been considered in equivalent circuit calculations, as the experimental values were between 0.87 and 0.93. Although the number of turns per phase N_{ms} is not symmetrical, it can be seen that power of each phase will be balanced, as the back-EMF is proportional to N_{ms} and, neglecting the stator resistance, the load resistance is proportional to $Z_s \cong X_s$, and therefore to N_{ms}^2.

$$P_{L4(EC)} = \sum_{m=1}^{4} \frac{E_{01(EC)}^2 R_L}{\left(R_s + R_L\right)^2 + \left(X_s + R_L \tan\varphi\right)^2} \tag{11}$$

$$E_{01(EC)} = k_n n \tag{12}$$

When iron losses are not considered, power balance in the equivalent circuit model is given by (13), where $P_{s4(EC)}$ are Joule losses in the stator resistance (14) and P_m are mechanical losses.

$$P_{in(EC)} = P_{L4(EC)} + P_{s4(EC)} + P_m \tag{13}$$

$$P_{s4(EC)} = \sum_{m=1}^{4} \frac{U_{s1(EC)}^2 R_s}{R_L^2 + X_L^2} \tag{14}$$

Mechanical losses P_m (15) are generally formed by bearing losses P_{mb}, windage losses in the rotor external surface P_{mw1} and windage losses in the rotor end surfaces P_{mw2}. In this work bearing losses have been determined using the bearing selector by SKF [34]. Besides, windage losses are due to friction between the rotor and surrounding air, and they have been determined using analytical formulae as a function of the Couette Reynolds number and the tip Reynolds number, respectively [35].

$$P_m = P_{mb} + P_{mw1} + P_{mw2} \tag{15}$$

C. Power Computations Using the Finite Element Method

Single-phase active power on the load $P_{L1(FEM)}$ is obtained by FEM software as (16), where $I_{s(FEM)}$ is the current through the load that is determined by FEM calculations, and $2\pi/p$ is the mechanical angle that corresponds to one electric period. As the time consumption of FEM simulations is very high for the proposed case studies (more than 48 hours in total), four-phase active power $P_{L4(FEM)}$ has been estimated from single-phase power using (17), considering that active power on the load is proportional to the stator voltage squared (8) and therefore to the number of turns squared, neglecting inner voltage drops. N_1 denotes the number of turns of phases 1 and 4, and N_2 is the number of turns of phases 2 and 3.

$$P_{L1(FEM)} = \frac{1}{2\pi/p} \int_0^{2\pi/p} R_L I_{s(FEM)}^2 \, \mathrm{d}\theta \tag{16}$$

$$P_{L4(FEM)} = 2P_{L1(FEM)} + 2\left(\frac{N_2}{N_1}\right)^2 P_{L1(FEM)} \quad (17)$$

In case of FEM simulations, power balance is given by (18). Four-phase Joule losses $P_{J4(FEM)}$ are calculated using (19), where $P_{hub}+P_{PM}$ are losses in the single-phase portion of the rotor hub and permanent magnet volumes (20), and $P_{s1(FEM)}$ are losses in the stator coil of phase 1, with N_1 turns and then resistance R_{s1} (21).

$$P_{in(FEM)} = P_{L4(FEM)} + P_{J4(FEM)} + 4P_{Fe1} + P_m \quad (18)$$

$$P_{J4(FEM)} = 4\left(P_{hub} + P_{PM}\right) + \left[2 + 2\left(\frac{N_2}{N_1}\right)^2\right] P_{s1(FEM)} \quad (19)$$

$$P_{hub} + P_{PM} = p\frac{1}{2\pi/p}\int_0^{2\pi/p}\int_{V_{hub}\cup V_{PM}} JE \,\mathrm{d}V \,\mathrm{d}\theta \quad (20)$$

$$P_{s1(FEM)} = \frac{1}{2\pi/p}\int_0^{2\pi/p} R_{s1} I^2_{s(FEM)} \,\mathrm{d}\theta \quad (21)$$

Computation of single-phase iron losses P_{Fe1} has been based on the model presented in [28]. In previous work this model was applied to the proposed TFM under no-load conditions [36], and here it is evaluated under load. This loss model ultimately aggregates alternating and rotational losses, that are in turn formed by hysteresis, eddy current and excess loss components obtained through a three-term empirical formula. The alternating loss coefficients of the TFM materials were determined experimentally, whereas circular rotational core losses were estimated from alternating losses, assuming that rotational versus alternating loss mechanisms are similar in the TFM materials and in a reference material (22).

$$\frac{p_r\left(f,\hat{B}\right)}{p_a\left(f,\hat{B}\right)} = \frac{p_{r(ref)}\left(f,\hat{B}\right)}{p_{a(ref)}\left(f,\hat{B}\right)} \quad (22)$$

Starting from the single-phase FEM model, the flux density at each volume element in cylindrical coordinates (B_r, B_t, B_z) is determined as the average value of all nodes within an element. Secondly, the *k*-th harmonics are calculated using Fourier analysis, and the axis ratios of their associated ellipses R_{Bk} are derived. Then specific losses (W/kg) p_{te} at each volume element are obtained from alternating and rotational losses p_{ak} and p_{rk}, adding up the contributions of all the *k*-th harmonics (23). Finally, total losses of a single phase P_{Fe1} in W fulfill (24), where p is the number of pole pairs of the machine, i. e. the number of periodicities in FEM model. ρ_e and V_e are the mass density and volume of each volume element in the FEM domain, with a total of N_e volume elements.

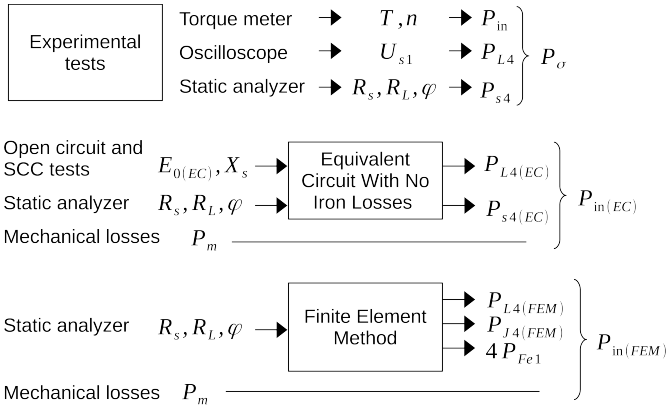

Figure 8: Flowchart of the analysis procedure

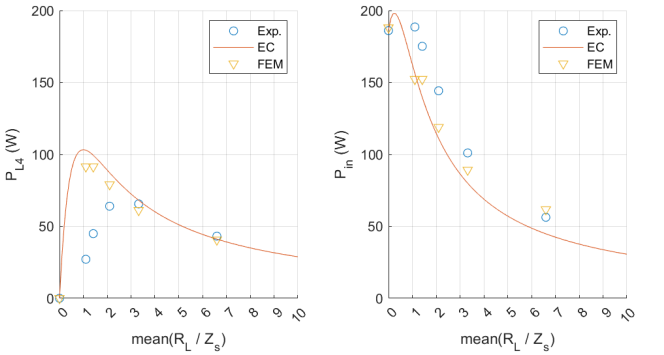

Figure 9: Power comparison at 400 r/min: (a) active power on the load, (b) input power

$$p_{te} = \sum_{k=0}^{\infty}\left[\left(1 - R_{Bk}\right)^2 p_{ak} + R_{Bk} p_{rk}\right] \quad (23)$$

$$P_{Fe1} = p\sum_{e=1}^{N_e} p_{te}\rho_e V_e \quad (24)$$

D. Comparison of Power Computations

The analysis procedure described in this section has been summarized in Fig. 8. Experimental data will be compared with results given by the equivalent circuit (EC) and the finite element method (FEM).

Fig. 9 and Fig. 10 compare active power and input power results at 400 and 5000 r/min, respectively, considering the three methods presented here: experimental tests, the EC and FEM. Moreover, Table III quantifies the accuracy of the EC and FEM through the mean absolute error (MAE) of computed powers.

At 400 r/min, i.e. low-speed tests, experimental active power on the load (Fig. 9a) seems to decline for those power values where $\mathrm{mean}\left(R_L/Z_s\right) < 3$, so when power is near its maximum value. This decline in experimental power on the load is a clear trend that is not captured by the EC and FEM and will be discussed in Section IV. Moreover, total input power does not decrease near the maximum power point (Fig.

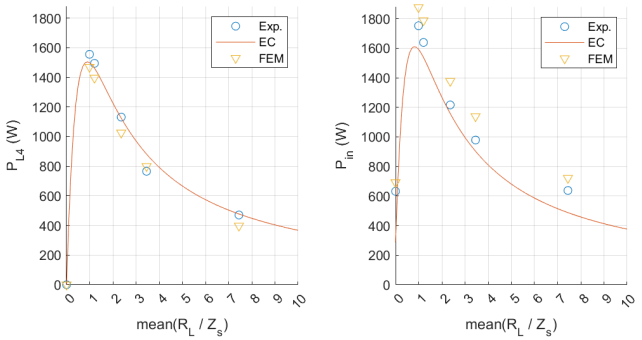

(a) (b)

Figure 10: Power comparison at 5000 r/min: (a) active power on the load, (b) input power

Table III: Mean absolute errors with respect to experimental values

	400 r/min	5000 r/min
$P_{L4(EC)}$	89.37 %	4.66 %
$P_{L4(FEM)}$	75.43 %	8.28 %
$P_{in(EC)}$	16.77 %	17.81 %
$P_{in(FEM)}$	12.04 %	11.41 %

9b), therefore it can be stated that computed input power is distributed experimentally among losses and active power on the load in a different way than expected.

On the other hand, results at 5000 r/min (Fig. 10) show a good agreement, with FEM having MAEs around 10 % when computing active power on the load and input power. At medium-speed the EC seems so predict load power with a very good accuracy, however, it predicts input power poorly.

IV. Analysis of Low-Speed Losses in the Transverse Flux Generator

In order to clarify load power discrepancies at 400 r/min near maximum power point, the following issues have been analyzed:

- Changes in the material properties due to the temperature rise (thermal effects). With the TFM rotating on the test rig under no load for 45 min, the temperature rise in the coil is measured using thermocouples that are integrated in the prototype. Fig. 11 shows experimental results, where the temperature rise has been depicted as a linear function of the no-load power. Then, it can be estimated that at 400 r/min the temperature rise after 45 min will be 2 °C, as experimental no-load losses are 11 W. Furthermore, the temperature rise at 5000 r/min is 78 °C. As agreement between experimental and computational results is much higher at 5000 r/min, involving higher power and temperature rise, thermal effects on the material properties can be neglected at 400 r/min.
- PMs model. The FEM model of magnets is linear (constant remanence and permeability), and should be accurate enough as PMs in the TFM prototype (Recoma 33E SmCo magnets by Arnold Magnetics) have a linear B-H curve at 20 °C [37] and the temperature rise at 400 r/min is negligible (Fig. 11). Electric conductivity is also included in FEM model in order to compute Joule losses in PM regions. Furthermore, demagnetization of PMs has been checked analytically, calculating the peak H-field $\hat{H}_{ad}$ produced by armature reaction in the d-axis (25). N_{ms} is the number of turns per phase, $\hat{I}_d$ is the peak current in the d-axis, g_d is the air gap in the d-axis and factor 2 is given by C-cores as the magnetic field crosses the air gap twice [4], [5]. In the worst case, i.e. short-circuit conditions, $\hat{H}_{ad}$ is lower than 50 kA/m, and according to the B-H curve of PMs it is a very low value in order to provoke demagnetization of PMs.

$$\hat{H}_{ad} = \frac{N_{ms}\hat{I}_d}{2g_d} \tag{25}$$

- SMC model. The stator material is Somaloy 130i 5P and the rotor material is Somaloy 700 HR 3P by Höganäs AB [38], [39]. SMC is characterized in the EC with a constant reactance, therefore assuming a linear material. Besides, in FEM domain it is modeled as an isotropic material with a nonlinear B-H curve, thus including saturation effects. According to experimental and FEM results, the back-EMF is linear with speed, so saturation effects can be neglected. Furthermore, hysteresis loops and electrical conductivity are not included in the FEM model, then iron losses (hysteresis, eddy current and anomalous losses) are calculated with a postprocessing script, as commonly done in FEM modeling of electrical machines.

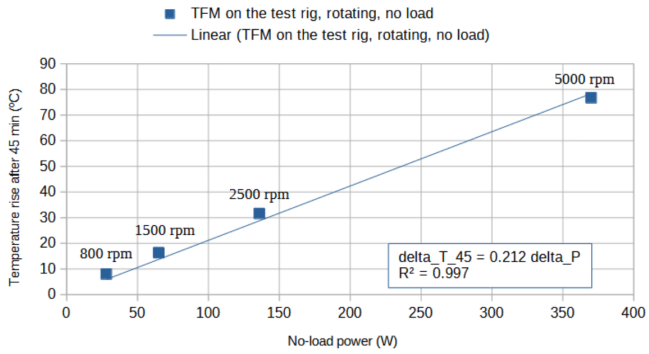

Figure 11: Experimental temperature rise after 45 min on the test rig versus no-load power at different speeds

A. Equivalent Circuit Including Core Losses

Analytical methods such as equivalent circuits are useful to model different physical phenomenon separately, such as the armature reaction and Joule losses. Besides, SMC materials typically have higher hysteresis losses than conventional steel laminations [11], this being of great importance at low frequencies, i.e. at 400 r/min. Therefore in this section the EC of Fig. 3 will be analyzed including core loss resistor R_{Fe}.

In EC models, iron losses $P_{Fe(EC)}$ are assumed to be proportional to the product of flux density and frequency squared, and therefore to resultant EMF $E_{r(EC)}$ squared [40], thus fulfilling (26).

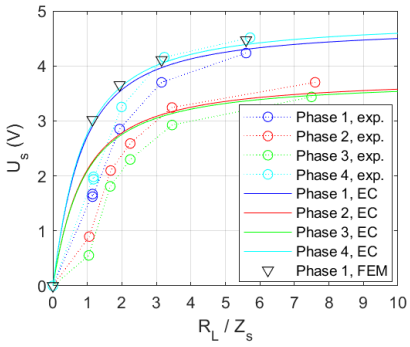

Figure 12: Stator voltage at 400 r/min

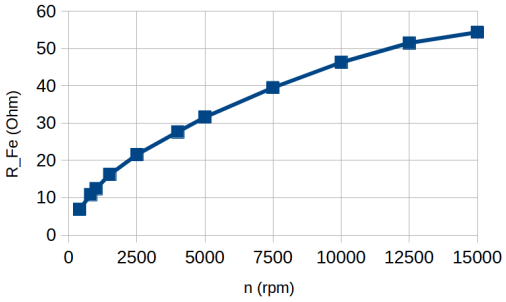

Figure 13: Core loss resistor changing with speed

$$P_{Fe(EC)} = \sum_{m=1}^{4} \frac{E_{r(EC)}^2}{R_{Fe}} \tag{26}$$

The expression of active power (27) according to the EC that includes iron losses (Fig. 3) shows that, once the impedances have been determined in a precise way, a decrease in active power can be explained by a decrease in the the resultant EMF $E_{r(EC)}$ (demagnetization). Moreover, terminal voltage at the load $U_{s1(EC)}$ follows (28). Thereby, a reduction in active power is correlated with a reduction in the resultant EMF, and so in the terminal voltage.

$$P_{L4(EC)} = \sum_{m=1}^{4} \frac{E_{r(EC)}^2 R_L}{\left(R_s + R_L\right)^2 + \left(X_\sigma + X_L\right)^2} \tag{27}$$

$$U_{s1(EC)} = E_{r(EC)} \frac{\sqrt{R_L^2 + X_L^2}}{\sqrt{\left(R_s + R_L\right)^2 + \left(X_\sigma + X_L\right)^2}} \tag{28}$$

Measurements of the terminal voltage (Fig. 12) confirm that experimental values are significantly lower than computed values for $R_L/Z_s < 3$, thus following the same trend as the load power (Fig. 9a). Moreover, this decrease in the terminal voltage indicates that real losses at the stator resistance in the TFM prototype are also lower than computed values, as the coil losses are proportional to the terminal voltage squared (9), (14).

Solving the equivalent circuit in Fig. 3 shows that the back-EMF and resultant EMF follow (29), where $|z|$ denotes the absolute value of complex number z, being $j = \sqrt{-1}$.

$$\frac{E_{0(EC)}}{E_{r(EC)}} = \left|1 + jX_m \left[\frac{1}{R_{Fe}} + \frac{1}{R_s + R_L + j\left(X_\sigma + X_L\right)}\right]\right| \tag{29}$$

Therefore, for a given magnetization from rotor PMs, i.e. for a given back-EMF $E_{0(EC)}$, a reduction of the resultant EMF in experiments with respect to expected values at low speeds can be explained by:

- An increase in magnetizing inductance X_m, i.e. a stronger armature reaction, due to non-linear magnetic performance of the stator SMC material with speed for low speed values.
- Iron losses resistor R_{Fe} decreasing at low speeds. Fig. 13 shows the iron losses resistor values that have been determined from experimental no-load losses $P_{0(exp)}$ using (12), (26). Results indicate that the core loss resistor is significantly reduced at low speeds, thus contributing to a reduction in the resultant EMF.

B. FEM and Experimental Power Segregation

FEM simulations include a more accurate model of SMC material, with a non-linear B-H curve and a three-term equation to calculate iron losses in postprocessing, taking into account high-order harmonics and rotational fields. Nevertheless, even with these improvements, FEM models do not capture the decrease in experimental load power at 400 r/min for high power cases.

Regarding experimental results, if both the load power and the coil losses are lower than expected, but not input power (Fig. 9b), it means that other losses P_σ have a greater contribution than expected in the TFM prototype. At such low speed (400 r/min, i.e. 80 Hz), Joule losses on PMs and the rotor hub do not have a significant effect, as well as mechanical losses, so the remaining component of P_σ are essentially iron losses on SMC materials.

Fig. 14 illustrates power segregation at 400 r/min from FEM and experimental values. Although total input power values are similar with both methods, power segregation is quite different. Experimental results prove that for those points that are near maximum power point production, P_σ losses that are dominated by iron losses are the biggest contribution to total input power by far, this contribution being much greater than predictions using conventional modeling. Besides, Fig. 15 shows experimental power validation at 5000 r/min, where the contribution of P_σ losses over total power is much lower, and therefore EC, FEM and experimental results have a better agreement.

V. Conclusion

The evaluation of core losses in SMC-based electrical machines is limited by the accuracy of calculation models, which have primarily been applied under no-load conditions. This restricts the understanding of loss mechanisms under varying

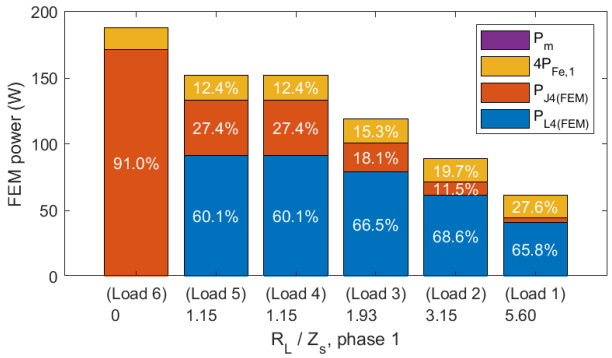

(a)

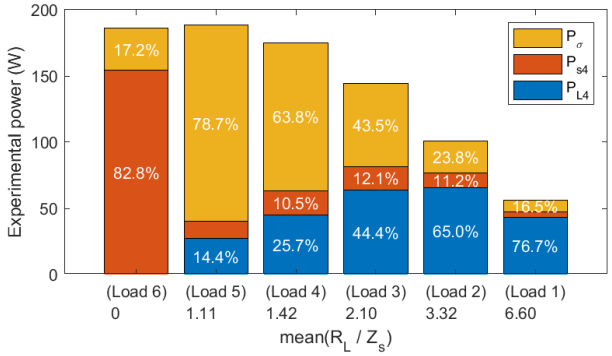

(b)

Figure 14: Power segregation at 400 r/min according to: (a) FEM, (b) experimental values

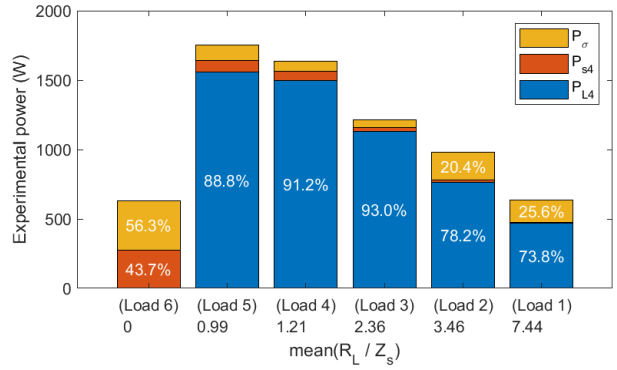

Figure 15: Power segregation at 5000 r/min according to experimental values

load conditions. Therefore, in this work a transverse flux generator (TFG) with SMC cores for aerospace applications has been modeled and tested at different speed and load conditions for a better comprehension of power and loss mechanisms. Conventional models, such as the equivalent circuit (EC) and the finite element method (FEM), have been compared with experimental results in order to analyze power segregation on the TFG.

Firstly, experimental tests have been conducted in order to determine the main parameters of the equivalent circuit, using a curve-fitting approach as the effects of the stator resistance cannot be neglected at low speeds in the TFG prototype. Furthermore, at 5000 r/min experimental and computational results of active power on the load and input power given by the EC and FEM show a good agreement. However, at 400 r/min there is a decline in experimental active power on the load near theoretical maximum power point, and this effect is not present in EC and FEM results.

Subsequently, conventional expressions of active power according to EC suggest that a decrease in the load power at low speed can be attributed to a reduction on the resultant electromotive force (demagnetization) and so on the terminal voltage. Measurements of the stator voltage have confirmed demagnetization in the TFG at 400 r/min. Furthermore, this phenomenon can be explained using the EC by a stronger armature reaction and a greater contribution of iron losses at low speeds. Power segregation from FEM and experimental results at 400 r/min confirms that remaining losses, dominated by iron losses on SMC materials, have a significant contribution to total input power. Therefore, power analyses presented in this work suggest that choosing a high-resistivity SMC material for the stator cores, with a good performance regarding high-speed losses, may entail some uncertainties for low-speed operation due to the magnetic behavior of SMC under load conditions.

REFERENCES

[1] V. Ballestín-Bernad, J. Artal-Sevil, and J. Domínguez-Navarro, "A review of transverse flux machines topologies and design," *Energies*, vol. 14, Nov. 2021.

[2] T. Husain, I. Hasan, Y. Sozer, I. Husain, and E. Muljadi, "A comprehensive review of permanent magnet transverse flux machines for direct drive applications," *2017 IEEE Energy Conversion Congress and Exposition (ECCE)*, pp. 1255–1262, Oct. 2017.

[3] W. Lee and G. Choi, "A Comprehensive Review of Fault-Tolerant AC Machine Drive Topologies: Inverter, Control, and Electric Machine," in *2021 IEEE 13th International Symposium on Diagnostics for Electrical Machines, Power Electronics and Drives (SDEMPED)*, vol. 1, pp. 269–275, Aug. 2021.

[4] V. Ballestín-Bernad, A. Egea-Cáceres, J. Artal-Sevil, and J. Domínguez-Navarro, "A Comprehensive Analytical Sizing Methodology for Transverse and Radial Flux Machines," *IEEE Access*, vol. 11, pp. 106063–106082, Sept. 2023.

[5] V. Ballestín-Bernad, *Design of a Novel Transverse Flux Electric Motor for Vehicle Traction Applications*. PhD, Universidad de Zaragoza, Zaragoza, Dec. 2023.

[6] D. Svechkarenko, *On Design and Analysis of a Novel Transverse Flux Generator for Direct-driven Wind Application*. PhD, KTH, School of Electrical Engineering, Stockholm, 2010. Publisher: KTH.

[7] A. M. El-Refaie, "Fault-tolerant permanent magnet machines: a review," *IET Electric Power Applications*, vol. 5, pp. 59–74, Jan. 2011. Publisher: IET Digital Library.

[8] M. U. Naseer, A. Kallaste, B. Asad, T. Vaimann, and A. Rassõlkin, "A Review on Additive Manufacturing Possibilities for Electrical Machines," *Energies*, vol. 14, p. 1940, Jan. 2021.

[9] R. Wrobel and B. Mecrow, "A Comprehensive Review of Additive Manufacturing in Construction of Electrical Machines," *IEEE Transactions on Energy Conversion*, vol. 35, pp. 1054–1064, June 2020.

[10] Y. Guo, X. Ba, L. Liu, H. Lu, G. Lei, W. Yin, and J. Zhu, "A Review of Electric Motors with Soft Magnetic Composite Cores for Electric Drives," *Energies*, vol. 16, p. 2053, Jan. 2023.

[11] N. Ahmed and G. J. Atkinson, "A Review of Soft Magnetic Composite Materials and Applications," *2022 International Conference on Electrical Machines, ICEM 2022*, pp. 551–557, 2022. ISBN: 9781665414326.

[12] T. Husain, I. Hasan, Y. Sozer, I. Husain, and E. Muljadi, "Design of a Modular E-Core Flux Concentrating Transverse Flux Machine," *IEEE Transactions on Industry Applications*, vol. 54, no. 3, pp. 2115–2128, 2018.

[13] A. Alaeddini, H. Tahanian, and A. Darabi, "Impact of Number of Phases on Electromagnetic Torque Characteristics of Transverse Flux Permanent Magnet Machines," *Advanced Electromagnetics*, vol. 8, no. 4, pp. 118–129, 2019.

[14] B. Boomiraja and R. Kanagaraj, "A novel hybrid flux machine with transverse flux stator and longitudinal flux rotor: Design and comparative analysis," *Electrical Engineering*, vol. 102, no. 3, pp. 1413–1422, 2020. ISBN: 0020202000967.

[15] M. C. Kulan, N. J. Baker, and S. Turvey, "Manufacturing challenges of a modular transverse flux alternator for aerospace," *Energies*, vol. 13, no. 6, 2020.

[16] M. C. Kulan, N. J. Baker, and S. Turvey, "Impact of Manufacturing and Material Uncertainties in Performance of a Transverse Flux Machine for Aerospace," *Energies*, vol. 15, Oct. 2022.

[17] S. Hieke, M. Stamann, D. Lagunov, R. Leidhold, A. Masliennikov, A. Duniev, and A. Yehorov, "Two-phase transverse flux machine with disc rotor for high torque low speed application," in *2017 19th European Conference on Power Electronics and Applications (EPE'17 ECCE Europe)*, pp. P.1–P.8, 2017.

[18] "TFM 8 - 3d printed Transverse Flux Generator by TanyaAkinora - Thingiverse," Jan. 2018. https://www.thingiverse.com/thing:2759924/makes. Accessed: 2024-6-12.

[19] A. Masliennikov, A. Yehorov, O. Duniev, R. Leidhold, M. Stamann, and S. Hieke, "The magnetic system analysis of the transverse flux machine and its improvement," *2019 IEEE 2nd Ukraine Conference on Electrical and Computer Engineering, UKRCON 2019 - Proceedings*, pp. 552–555, July 2019. ISBN: 9781728138824.

[20] V. Ballestín-Bernad, J. Artal-Sevil, and J. Domínguez-Navarro, "Prototype of a Two-Phase Axial-Gap Transverse Flux Generator Based on Reused Components and 3D Printing," *Energies*, vol. 16, Feb. 2023.

[21] Y. Guo, J. Zhu, J. Zhong, and W. Wu, "Core losses in claw pole permanent magnet machines with soft magnetic composite stators," in *Digest of INTERMAG 2003. International Magnetics Conference (Cat. No.03CH37401)*, (Boston, MA, USA), pp. EA–11, IEEE, 2003.

[22] Y. G. Guo, J. G. Zhu, J. J. Zhong, P. A. Watterson, and W. Wu, "An improved method for predicting magnetic power losses in SMC electrical machines," *International Journal of Applied Electromagnetics and Mechanics*, vol. 19, pp. 75–78, May 2004.

[23] Y. G. Guo, J. G. Zhu, P. A. Watterson, and W. Wu, "Development of a permanent magnet claw pole motor with soft magnetic composite core," *Australian Journal of Electrical and Electronics Engineering*, vol. 2, no. 1, pp. 21–30, 2005.

[24] V. Ballestín-Bernad, M. Kulan, N. Baker, and J. Artal-Sevil, "Loss Analysis of a Soft Magnetic Composite Transverse Flux Machine," in *IET Conference Proceedings*, (Brussels, Belgium), pp. 283–290, IET, Oct. 2023.

[25] A. Krings and J. Soulard, "Overview and Comparison of Iron Loss Models for Electrical Machines," *Journal of Electrical Engineering*, vol. 10, pp. 162–169, May 2010.

[26] Z.-Q. Zhu, S. Xue, W. Chu, J. Feng, S. Guo, Z. Chen, and J. Peng, "Evaluation of Iron Loss Models in Electrical Machines," *IEEE Transactions on Industry Applications*, vol. 55, pp. 1461–1472, Mar. 2019.

[27] Y. J. Li, Q. X. Yang, Y. H. Wang, J. G. Zhu, and Z. W. Lin, "Rotational core loss features of soft magnetic composite materials under excitation frequencies from 5 Hz to 1000 Hz," in *2013 IEEE International Conference on Applied Superconductivity and Electromagnetic Devices*, pp. 450–453, Oct. 2013.

[28] Y. Guo, J. Zhu, H. Lu, Z. Lin, and Y. Li, "Core Loss Calculation for Soft Magnetic Composite Electrical Machines," *IEEE Transactions on Magnetics*, vol. 48, pp. 3112–3115, Nov. 2012.

[29] Y. Guo, J. G. Zhu, P. Watterson, and W. Wu, "Development of a PM transverse flux motor with soft magnetic composite core," *IEEE Transactions on Energy Conversion*, vol. 21, pp. 426–434, June 2006.

[30] J. G. Zhu, Y. G. Guo, Z. W. Lin, Y. J. Li, and Y. K. Huang, "Development of PM Transverse Flux Motors With Soft Magnetic Composite Cores," *IEEE Transactions on Magnetics*, vol. 47, pp. 4376–4383, Oct. 2011.

[31] N. J. Baker, D. J. B. Smith, M. C. Kulan, and S. Turvey, "Design and Performance of a Segmented Stator Permanent Magnet Alternator for Aerospace," *IEEE Transactions on Energy Conversion*, vol. 33, pp. 40–48, Mar. 2018.

[32] Ideal Magnet Solutions, "Samarium Cobalt vs Neodymium Magnets," May 2019. https://idealmagnetsolutions.com/knowledge-base/samarium-cobalt-vs-neodymium-magnets/. Accessed: 2024-9-16.

[33] "IEC 60034-4-1:2018. Rotating electrical machines - Part 4-1: Methods for determining electrically excited synchronous machine quantities from tests."

[34] SKF, "SKF Bearing Select." https://skfbearingselect.com/#/bearing-selection-start. Accessed: 2024-04-19.

[35] J. Pyrhonen, T. Jokinen, and V. Hrabovcova, *Design of Rotating Electrical Machines*. John Wiley & Sons, Feb. 2009.

[36] V. Ballestín-Bernad, M. C. Kulan, N. J. Baker, and J. A. Domínguez-Navarro, "No-Load Loss Computations in a Transverse Flux Generator with Soft Magnetic Composites," 2024. Unpublished.

[37] Arnold Magnetic Technologies, "Samarium Cobalt Magnets." https://www.arnoldmagnetics.com/products/recoma-samarium-cobalt-magnets/. Accessed: 2024-6-10.

[38] Höganäs AB, "Somaloy 5P," 2024. https://www.hoganas.com/en/powder-technologies/products/somaloy/somaloy-5p/ Accessed: 2024-04-26.

[39] Höganäs AB, "Somaloy 3P," 2024. https://www.hoganas.com/en/powder-technologies/products/somaloy/somaloy-3p/ Accessed: 2024-04-26.

[40] R. Krishnan, *Permanent Magnet Synchronous and Brushless DC Motor Drives*. CRC Press, 2010.